Synthesis and electronic properties of epitaxial math xmlns="http://www.w3.org/1998/Math/MathML">mrow>msub>mi mathvariant="normal">SrNiO/mi>mn>3/mn>/msub>mo>//mo>msub>mi mathvariant="normal">SrTiO/mi>mn>3/mn>/msub>/mrow>/math> superlattices

Le Wang, Jiali Zhao, Cheng-Tai Kuo, Bethany E. Matthews, Marjolein T. Oostrom, Steven R. Spurgeon, Zhenzhong Yang, Mark E. Bowden, Linda W. Wangoh, Sang-Jun Lee, Jun-Sik Lee, Er-Jia Guo, Jiaou Wang, Scott A. Chambers, and Yingge Du

Phys. Rev. Materials **6**, 075006 — Published 20 July 2022

DOI: 10.1103/PhysRevMaterials.6.075006

Synthesis and Electronic Properties of Epitaxial $SrNiO_3/SrTiO_3$ Superlattices

Le Wang[1,*], Jiali Zhao[2,3], Cheng-Tai Kuo[4], Bethany E. Matthews[5], Marjolein T. Oostrom[6], Steven R. Spurgeon[5,7], Zhenzhong Yang[1], Mark E. Bowden[8], Linda W. Wangoh[1], Sang-Jun Lee[4], Jun-Sik Lee[4], Er-Jia Guo[3], Jiaou Wang[2], Scott A. Chambers[1], and Yingge Du[1,*]

[1]Physical and Computational Sciences Directorate, Pacific Northwest National Laboratory, Richland, Washington 99354, USA
[2]Beijing Synchrotron Radiation Facility, Institute of High Energy Physics, Chinese Academy of Sciences, Beijing, 100039 China
[3]Beijing National Laboratory for Condensed Matter Physics and Institute of Physics, Chinese Academy of Sciences, Beijing 100190, China
[4]Stanford Synchrotron Radiation Lightsource, SLAC National Accelerator Laboratory, Menlo Park, California 94025, USA
[5]Energy and Environment Directorate, Pacific Northwest National Laboratory, Richland, Washington 99352, USA
[6]National Security Directorate, Pacific Northwest National Laboratory, Richland, Washington 99352, USA
[7]Department of Physics, University of Washington, Seattle, Washington 98195, USA
[8]Environmental Molecular Sciences Laboratory, Pacific Northwest National Laboratory, Richland, Washington 99352, USA

[*]Authors to whom correspondence should be addressed: le.wang@pnnl.gov; yingge.du@pnnl.gov

Abstract: We report the deposition and characterization of a set of atomically precise $(SrNiO_3)_1/(SrTiO_3)_n$ superlattices using oxide molecular beam epitaxy. We demonstrate that one unit cell of $SrNiO_3$ can be stabilized as a perovskite in these structures and that there is no charge transfer across the heterointerface. Detailed spectroscopy data analysis indicates that holes are confined to the $SrNiO_3$ unit cells, resulting in a Ni valence between 3 and 4. Hole hopping conductivity is observed in the $n = 1$ superlattice but is strongly suppressed along the *c*-axis direction for $n = 3$ and 5, resulting in the insulting behavior in the latter. Our study will inspire the epitaxial synthesis of $(SrNiO_3)_1/(RNiO_3)_n$ superlattices, as measurements of their properties could open a new platform for studying nickelate-based superconductors.

Keywords: superlattice, quantum confinement, nickelates, charge transfer, $SrNiO_3$

ABO_3-type perovskite oxides have sufficient structural flexibility to generate a wide range of functional properties for electronics and energy storage applications [1-4]. First-row transition

metals are the most extensively studied *B*-site elements in these materials. Almost all the transition metals have multiple oxidation states since they readily lose valence electrons to form stable cations [5]. For Ni, the most stable oxidation state is Ni^{2+} resulting in NiO being the only stable binary oxide of Ni. Advances in thin-film growth technologies make it possible to synthesize stable rare-earth nickelates $RNiO_3$ (*R*NO, where *R* represents a rare-earth lanthanide element) thin films in which Ni is trivalent. Due to the recent discovery of superconductivity in reduced infinite layer $R_{1-x}Sr_xNiO_2$ thin films [6-11], *A*-site aliovalent substitution of Sr^{2+} for R^{3+} in the parent *R*NO perovskite has generated intense scientific interest within the synthesis community. In the absence of oxygen vacancies, Ni assumes a less stable formal charge, $3+x$, in $R_{1-x}Sr_xNiO_3$. It is thus challenging to synthesize stable, stoichiometric $R_{1-x}Sr_xNiO_3$ thin films, particularly at high Sr concentration ($x > 0.3$) [12].

In contrast to perovskite *R*NO, $SrNiO_3$ (SNO) is expected to form a hexagonal structure as the small ionic radius of Ni^{4+} ion leads to a Goldschmidt tolerance factor (t) greater than unity. Previous first-principles density-functional theory (DFT) calculations predict that hexagonal SNO is a ferromagnetic half-metal with promising applications in spintronic devices [13]. Although bulk hexagonal SNO has been synthesized under high pressure ($P_{O2} > 50$ atm) [14], there was no data to support the presence of Ni^{4+} in this lattice. It was also reported that the cubic perovskite $SrFe_{1-x}Ni_xO_3$ ($0 \leq x \leq 0.5$) can be stabilized under high-pressure and high-temperature conditions although extensive NiO secondary phase formation was observed for $x > 0.5$ [15]. The cubic lattice parameter (~ 3.81 Å) for bulk SNO was extracted from a linear fit of the lattice parameter dependence on x [15]. Our recent efforts to stabilize SNO thin films on perovskite substrates by oxide molecular beam epitaxy (MBE) led to spontaneous phase segregation. As a

result, two co-existing, oxygen-deficient Ruddlesden-Popper phases (Sr_2NiO_3 and $SrNi_2O_3$) were observed [16].

By limiting the SNO layer thickness at the single unit cell (u.c.) level, we have demonstrated that cubic perovskite structured SNO can be stabilized when incorporated into superlattices (SL) with $LaFeO_3$ (LFO) [17]. However, strong overlap between the Ni 2*p* and La 3*d* X-ray photoemission core levels precludes obtaining clean Ni 2*p* spectra, and large lattice distortions from LFO layers obscure the intrinsic structural and electronic properties of SNO. Here we replace LFO with $SrTiO_3$ (STO) to form the SNO/STO SLs (**Figure 1a**). The reason for choosing STO is fourfold. First, both Ti 2*p* X-ray photoelectron spectroscopy (XPS) and Ti *L* edge X-ray absorption spectroscopy (XAS) features are well separated from the analogous Ni spectra. Second, cubic STO (a_c=3.905 Å) without any oxygen octahedral rotations (OORs) and/or *A*-site displacements provides a good structural/symmetry match for single-layer SNO. Third, there is no polarity difference between the two (non-polar) materials, SNO and STO. Finally, tetravalent (formally $3d^0$) Ti is exceedingly stable in STO under all environmental conditions [18]. As a result, charge transfer is not expected to occur at the SNO/STO interface and the intrinsic electronic properties of SNO should be preserved.

We examine the structural and electronic properties of SNO_1/STO_n SLs synthesized by oxide MBE in which the STO layer thickness (*n*) is varied from 1 to 5 u.c. The characterization results are compared with those of pure STO and solid solution $SrTi_{0.5}Ni_{0.5}O_{3-\delta}$ (STNO) thin films. X-ray diffraction (XRD) and scanning transmission electron microscopy (STEM) measurements confirmed the high crystalline quality of these SNO_1/STO_n SLs. *In situ* XPS and *ex situ* XAS were used to probe the interface electronic structure and valences of the B-site cations (Ni and Ti). Our results reveal that the Ni valence for SNO_1/STO_n SLs exceeds 3+ but is

not 4+, whereas the Ti valence is 4+. These formal charges do not change with *n*, indicating that there is no charge transfer across the SNO/STO interface. Valence band offset (VBO) analysis further demonstrates that holes are confined to the SNO layers, consistent with the hole hopping conduction mechanism revealed by in-plane transport measurements. Our findings have significant implications for the controlled engineering of Ni valence in complex nickelates.

A set of SNO_1/STO_n SLs, one 30 nm thick STO film, and one 10 nm thick STNO film were deposited on (001)-oriented $(LaAlO_3)_{0.3}(Sr_2AlTaO_6)_{0.7}$ (LSAT) substrates by oxide MBE with assistance of *in situ* reflection high-energy electron diffraction (RHEED) to monitor the growth (see Experimental Methods of the **Supplementary Materials** [19]). LSAT with its pseudo-cubic lattice constant of ~3.868 Å was used as the substrate because of its small in-plane lattice mismatch with STO and SNO. To stabilize the perovskite phase SNO in SLs [17], the SNO layer thickness was set to one u.c. while *n* varies from 1 to 3 to 5 u.c. The clear RHEED intensity oscillations during the growth (**Figure 1b**) demonstrate a two-dimensional (2D) layer-by-layer film growth mode. The RHEED patterns of SNO_1/STO_n SLs after growth (**Figure 1c**) exhibit sharp, bright streaks characteristic of the desired perovskite structure and no additional diffraction spots that would otherwise indicate the presence of secondary phases. In contrast, the RHEED pattern of the STNO solid solution indicates a much rougher surface and a mix of phases (see **Figure S1** of the **Supplementary Materials** [19]). **Figure 1d** shows high-resolution XRD θ–2θ scans in the vicinity of the LSAT(002) peak for the SLs and pure STO film. The presence of clear SL Bragg peaks and SL thickness fringes indicates good crystallinity. Representative X-ray reflectivity (XRR) scans and related modeling (see **Figure S2** of the **Supplementary Materials** [19]) further confirm the overall structural quality of these SLs. All SLs and pure STO film were found to be coherently strained to LSAT according to reciprocal

space maps (RSMs) (**Figure 1e**). The SL Bragg angle shifts to a higher 2θ value with decreasing n in SNO_1/STO_n SLs, indicating that the average out-of-plane lattice constant (c) decreases. As shown in **Figure 1f**, c decreases almost linearly with increasing contribution from the SNO layers in SNO_1/STO_n SLs. A linear fit shows a c value of ~ 3.78 Å for pure SNO, smaller than that (~ 3.81 Å) of bulk cubic SNO due to the tensile strain effect imposed by the LSAT substrate, confirming that the cubic perovskite phase SNO was successfully stabilized in these SNO_1/STO_n SLs. On the other hand, the c value of the STNO solid solution is much larger than that of the n = 1 SL, indicating the likely formation of oxygen vacancies in STNO as a result of the instability of high Ni valence states.

To better understand the local crystal structure and OOR behavior for the SNO_1/STO_n SLs, we performed STEM measurements. A schematic diagram for a n = 1 SL deposited on a buffer layer of 5 u.c. STO is seen in **Figure 2a**. **Figure 2b** shows the template-matched STEM annular dark field (ADF), annular bright field (ABF), and inverted ABF (IABF) images for a typical n = 1 SL. The expected epitaxial relationship is clearly present, and the interfaces are free of dislocations. However, atomic-scale electron energy loss spectroscopy (EELS) maps of a representative n = 5 SL (see **Figure S3** of the **Supplementary Materials** [19]) reveal some *B*-site cation interdiffusion across the SNO/STO interface. Here we measure *B*-site and O sublattice displacements to estimate the degree of OOR, as shown in **Figure 2c** and **Figure S4** of the **Supplementary Materials** [19]. We observe substantial sublattice displacements (8–10 pm) in the 5 u.c. STO buffer, but only 5–6 pm in the first half of the SL and essentially zero at the crystal surface. This overall trend agrees with the expected strain near the buffer and potential relaxation at the sample surface. We note that 2–3 pm displacements are also measured in the LSAT substrate for which the displacements are nominally zero, suggesting that the uncertainty

in the SL displacements is ± 3 pm. Thus, the SL displacements are 6 ± 3 pm, which are nearly negligible [20]. Furthermore, some beam-induced damage is visible in the topmost layers of the crystal which may impact the displacement measurements there. Increasing n in SNO_1/STO_n SLs causes the structural properties of the STO layers to approach those of bulk STO (**Figure 1d** and **Figure 1f**). Thus, the oxygen displacements and associated OORs are negligible in these SNO_1/STO_n SLs, different with the SNO_1/LFO_n SLs in which LFO layers strongly affect the OORs and then tune the B-site cation valences [17].

To study the effect of n on the B-site cation valences in SNO_1/STO_n SLs, *in situ* XPS and *ex situ* XAS measurements were performed. A plasma-annealed $NdNiO_3$ film (PA-NNO) was used as a Ni^{3+} standard and a vacuum-annealed $NdNiO_{3-\delta}$ film (VA-NNO), a Sr_2NiO_3 film, and a NiO film were used as Ni^{2+} standards [16]. It is well known that Ni 2*p* XPS and *L*-edge XAS line shapes in transition metal (TM)-containing oxides can exhibit multiplet fine structure due to angular momentum coupling of the unpaired 3*d* valence electrons to the unpaired 2*p* core electron following 2*p* photoionization [21-22]. Additionally, in the case of XPS, valence charge arrangement in response to the strong electronic perturbation generated by core-hole creation ("shake" phenomena) leading to prominent charge-transfer (CT) satellite peaks not seen in spectra for the pure TM element is quite common in oxides containing TM cations [23]. CT satellites are generally weak in XAS due to screening of the core hole by the excitonic final state [24]. The different local atomic and electronic structures found in different crystal lattices can result in very different Ni 2*p* XPS and *L*-edge XAS.

Figure 3a shows Ni 2*p* XPS spectra for the three SLs, STNO, and the four reference samples mentioned above. All spectra were shifted so the corresponding O 1*s* peaks fall at 530.0 eV. The spectra for SNO_1/STO_n SLs are very similar, and their line shapes closely resemble that

of PA-NNO. The Ni $2p_{3/2}$ features for SNO_1/STO_n SLs are shifted to slightly higher binding energy (~0.2 eV) relative to that of PA-NNO. This result suggests that the Ni valence in the SNO_1/STO_n SLs may slightly exceed 3+. However, the Ni valence is clearly not 4+ as the chemical shift in both XPS and XAS peak centroids is roughly +1 eV per unit increase in valence for most of the 3*d* transition metal (TM) oxides [25-30]. In contrast, the Ni 2*p* spectrum for STNO is very similar to that for VA-NNO, and the Ni $2p_{3/2}$ feature peak energy is the same as that of VA-NNO and Sr_2NiO_3, indicating that the Ni valence in STNO is Ni^{2+}. It is noteworthy that the primary $j = 3/2$ and 1/2 spin-orbit components in the Ni 2*p* spectrum for rock salt NiO fall at significantly lower binding energies than those for the perovskites Sr_2NiO_3 and VA-NNO despite the three materials containing Ni with nominally the same valence. This result indicates that the practice of calibrating the Ni 2*p* spectra using a constant O 1*s* binding energy of 530.0 eV may not be reliable when going from one lattice structure to another.

The Ni valence assignment from Ni 2*p* XPS is corroborated by XAS measurements at the Ni *L*-edge. As shown in **Figure 3b**, we compare the Ni *L*-edge XAS for SNO_1/STO_n SLs and STNO with those of reference samples of PA-NNO (Ni^{3+} valence state) and NiO (Ni^{2+} valence state). For PA-NNO, there are two distinct peaks at the Ni L_3 edge (labeled α and β), located at 853.3 and 854.3 eV, respectively, and a single feature located at ~871.6 eV at the Ni L_2 edge. NiO spectrum shows a two-peak structure at both the L_3 and L_2 edges and the spectral feature at L_3 edge shows a sharp increase (decrease) in the intensity of peak α (β) as well as a shift to lower (higher) photon energy relative to PA-NNO. The Ni *L*-edges for the SNO_1/STO_n SLs are similar to that of PA-NNO except the feature of β. At both the L_3 edge and L_2 edge, corresponding β features slightly shift toward higher photon energy compared to the Ni^{3+} reference (PA-NNO). This indicates that the Ni valence for SNO_1/STO_n SLs exceeds 3+, which is consistent with our

XPS results shown in **Figure 3a**. We note that the spectral weight of feature α at the Ni L_3 edge for the n = 1 SL is comparable to that of feature β, suggesting that the average Ni valence for the n = 1 SL is lower than that for the n = 3 and 5 SLs [29, 31-32]. The lower Ni valence for the n = 1 SL is likely associated with some degree of Ni/Ti intermixing and/or air exposure and degradation before XAS measurements. We also compare the Ni *L*-edge XAS for the n = 1 SL and the STNO solid solution. The Ni spectrum of the STNO solid solution is very similar to that of NiO, indicating that the Ni valence state in STNO is Ni^{2+}, consistent with the larger c value deduced from XRD (**Figure 1f**), and highlighting the differences between the SL and the solid solution with the same volume-averaged composition. **Figure S5** of the **Supplementary Materials** [19] displays the normalized Ti *L*-edge XAS of SNO_1/STO_n SLs. No changes in peak shape and peak position are observed when changing n. The Ti *L*-edge XAS are in good agreement with that previously reported for pure STO [33], confirming that the Ti valence in SNO_1/STO_n SLs is Ti^{4+}. Thus, all the above spectroscopic data confirm that there is no charge transfer across the STO/SNO interface.

For 3*d* TM oxides, increasing the valence of the TM cation lowers the absorption energy of its 3*d* unoccupied states. When TM is bonded with oxygens, it undergoes TM 3*d*-O 2*p* hybridization, resulting in a lower X-ray absorption energy for the O *K* pre-edge peak. For example, a higher TM oxidation state gives rise to a lower O *K* pre-edge peak energy [34]. Thus, the pre-edge spectral feature at O *K*-edge is very sensitive to monitoring changes in the TM oxidation state. In this fashion, we carried out the O *K* pre-edge features for these SNO_1/STO_n SLs to further scrutinize the Ni valence. As shown in **Figures 3c-d**, the O *K* pre-edge peaks for SNO_1/STO_n SLs are located at the same photon energy (about 527.8 eV), which is slightly lower than the pre-edge peak for PA-NNO (about 528 eV). This pre-edge feature is consistent with a

Ni oxidation state slightly higher than 3+ in the SLs [34]. Moreover, the O *K* pre-edge peak width for SNO_1/STO_n SLs is greater than that for PA-NNO (**Figure 3d**), suggesting a stronger Ni 3*d*–O 2*p* hybridization for SNO layers in SNO_1/STO_n SLs [35], further supporting that the Ni valence for SNO_1/STO_n SLs is higher than 3+.

Figure 4a shows the valence band (VB) spectra for three SNO_1/STO_n (n = 1, 3, 5) SLs along with that of pure STO film. All spectra were shifted such that the corresponding Ti $2p_{3/2}$ peaks fall at the same binding energy as that for pure STO film. Three SLs show the same VB maximum (VBM) value (~2.1 eV), which is smaller than that of pure STO film by ~1 eV. Determining accurate VB offsets (VBOs) from XPS as described by Kraut *et al.* [36] is precluded by the fact that a reference specimen of thick-film perovskite SNO could not be synthesized due to its instability [16]. Here we utilize an approximate method instead. Based on the observation that the VBM values of the SLs are lower in binding energy than that of pure STO film, we intuit that the top portions of the SL VBs are SNO derived [17]. As a result, the VBO can be estimated as $\Delta E_V \approx E_V(\text{STO}) - E_V(\text{SL})$. The same VBM value for different n in SNO_1/STO_n SLs leads to the same ΔE_V value (~1.0 eV). Thus, holes are confined to the SNO layers in SNO_1/STO_n SLs **(Figure 4b**). **Figure 4c** shows resistivity versus temperature (ρ-T) curves for the n = 1 SL and the reference PA-NNO film. The n = 3 and 5 SLs are too resistive to measure with our current experimental setup. The reference PA-NNO film shows metallic bulk-like ρ-T behavior with low resistivity of $\sim 3.2\times10^{-4}$ Ω.cm at 300 K, while the n = 1 SL exhibits semiconducting behavior with high resistivity of 0.52 Ω.cm at 300 K.

To gain further insight into the conduction mechanism for these SLs, the transport behavior of the n = 1 SL was fitted to two different models as shown in **Figure 4d-e**. Attempts to fit the ρ-T curve for the n = 1 SL to a simple activated model [$\rho=\rho_0\exp(E_A/k_BT)$] failed, as there is a clear

curvature in the Arrhenius plot (**Figure 4d**). We note that variable range hopping (VRH) type of conduction has been observed in both ultrathin RNO films and several RNO-based SLs [37-39]. Thus, VRH model [$\rho=\rho_0 exp(T_0/T)^{\alpha}$] was also used to fit the ρ-T curve of the n = 1 SL. As seen in **Figure 4e**, both two dimensional 2D (α=1/3) and 3D (α=1/4) VRH models fit well, suggesting that conduction in SNO_1/STO_n SLs is due to holes hopping in SNO layers. The SNO_1/STO_n SL can be considered as a periodic set of multiple quantum wells in which n u.c. STO layers separate the individual wells (see schematic in **Figure 4b**). For the n = 1 SL, since carriers (holes here) can tunnel through the barriers between quantum wells and the wave functions of neighboring wells couple together, the electronic states form delocalized minibands and semiconducting behavior was observed. With increasing n from 1 to 3 and 5, barriers between quantum wells become wider enough such that carriers cannot tunnel through, which strongly suppresses hole hopping along the c-axis direction [40] and makes the system more localized and insulating.

We also measured the magnetic properties of these SLs. No obvious magnetic moment is observed over the temperature range 5 to 300 K (not shown here). Whereas, recent DFT simulations indicated that ferromagnetic coupling exists between the Ni cations of the cubic perovskite $SrNiO_{3-\delta}$ and that the removal of oxygen (i.e. larger δ) increases the net magnetization [41]. Insertion of STO layers between ultrathin SNO layers in our SNO/STO SLs breaks the long-range ferromagnetic coupling that exists in pure SNO, presumably resulting in the absence of ferromagnetism we have observed.

In summary, we have synthesized a series of SNO_1/STO_n SLs grown on (001)-oriented LSAT substrates by oxide MBE and investigated the effect of n on lattice structure, electronic properties, and transport behavior. We found that SNO_1/STO_n SLs exhibit high structural quality

and are coherently strained to LSAT substrates. The Ti valence is 4+ while the Ni valence exceeds 3+ but is not 4+, and neither valence changes with *n*. In contrast, the STNO solid solution exhibits low structural quality and lots of oxygen vacancies, driving the Ni valence down to 2+. In-plane transport data are consistent with variable-range hole hopping conductivity for the $n = 1$ SL. However, hole hopping along the *c*-axis direction was strongly suppressed when increasing *n* to 3 and 5, resulting in insulating behavior. Our work further highlights that the structural environment of complex materials can be controlled to achieve electronic structures that are not found in analogous bulk materials by means of SL formation. It is thus of interest to use the same approach to synthesize the SNO_1/RNO_n SLs and compare the resulting electronic properties and transport data to that of solid solutions with the same volume-averaged composition, *i.e.*, $R_{1-x}Sr_xNiO_3$ where $x = 1/(n+1)$. Doing so may open new avenues for studying superconductivity in nickel-based oxides. Ongoing studies in our lab are investigating the impact of strain and lattice orientation on the structure and properties of $SrNiO_3$ films and heterostructures. Further experimental investigations will address how to suppress the formation of oxygen vacancies during the growth and/or cooling process for $SrNiO_3$ films.

Acknowledgements

This work was supported by the U.S. Department of Energy (DOE), Office of Science, Office of Basic Energy Sciences, Division of Materials Sciences and Engineering under Award #10122. We acknowledge facility support from W. R. Wiley Environmental Molecular Sciences Laboratory, a DOE User Facility sponsored by the Office of Biological and Environmental Research. We thank Dr. Peter V. Sushko for valuable discussions. The soft x-ray spectroscopy experiments were carried out at the SSRL (beamline 13-3), SLAC National Accelerator Laboratory, supported by the U.S. Department of Energy, Office of Science, Office of Basic Energy Sciences under contract no. DE-AC02-76SF00515. Part of this work was carried out with the support of 4B9B beamline at Beijing Synchrotron Radiation Facility. A portion of the

microscopy work was performed in the Radiological Microscopy Suite (RMS), located in the Radiochemical Processing Laboratory (RPL) at PNNL.

Competing interests

The authors declare no competing financial interests.

Additional information

Supporting Information is available online or from the author.

References

1. N. Reyren, S. Thiel, A.D. Caviglia, L. Fitting Kourkoutis, G. Hammerl, C. Richter, C. W. Schneider, T. Kopp, A.-S. Ruetschi, D. Jaccard, M. Gabay, D. A. Muller, J.-M. Triscone, and J. Mannhart, Science **317**, 1196 (2007).
2. I. Grinberg, D. Vincent West, M. Torres, G. Gou, D. M Stein, L. Wu, G. Chen, E. M. Gallo, A. R. Akbashev, P. K. Davies, J. E. Spanier, and A. M. Rappe, Nature **503**, 509 (2013).
3. Y. Zhou, X. Guan, H. Zhou, K. Ramadoss, S. Adam, H. Liu, S. Lee, J. Shi, M. Tsuchiya, D. D. Fong, and S. Ramanathan, Nature **534**, 231 (2016).
4. J. Hwang, R. R. Rao, L. Giordano, Y. Katayama, Y. Yu, and Y. Shao-Horn, Science **358**, 751 (2017).
5. H. Raebiger, S. Lany, and A. Zunger, Nature **453**, 763 (2008).
6. D. Li, K. Lee, B. Y. Wang, M. Osada, S. Crossley, H. R. Lee, Y. Cui, Y. Hikita, and H. Y. Hwang, Nature **572**, 624 (2019)
7. Q. Gu, Y. Li, S. Wan, H. Li, W. Guo, H. Yang, Q. Li, X. Zhu, X. Pan, Y. Nie, and H. H. Wen, Nat. Commun. **11**, 6027 (2020).
8. D. Li, B. Y. Wang, K. Lee, S. P. Harvey, M. Osada, B. H. Goodge, L. F. Kourkoutis, and H. Y. Hwang, Phys. Rev. Lett. **125**, 027001 (2020).
9. M. Osada, B. Y. Wang, B. H. Goodge, K. Lee, H. Yoon, K. Sakuma, D. Li, M. Miura, L. F. Kourkoutis, and H. Y. Hwang, Nano Lett. **20**, 5735 (2020).
10. S. Zeng, C. S. Tang, X. Yin, C. Li, M. Li, Z. Huang, J. Hu, W. Liu, G. J. Omar, H. Jani, Z. S. Lim, K. Han, D. Wan, P. Yang, S. J. Pennycook, A. T. S. Wee, and A. Ariando, Phys. Rev. Lett. **125**, 147003 (2020).
11. M. Osada, B. Y. Wang, B. H. Goodge, S. P. Harvey, K. Lee, D. Li, L. F. Kourkoutis, and H. Y. Hwang, Adv. Mater. **33**, 2104083 (2021).
12. K. Lee, B. H. Goodge, D. Li, M. Osada, B. Y. Wang, Y. Cui, L. F. Kourkoutis, and H. Y. Hwang, APL Mater. **8**, 041107 (2020).
13. G. Y. Chen, C. L. Ma, D. Chen, and Y. Zhu, J. Solid State Chem. **233**, 438 (2016).
14. Y. Takeda, T. Hashino, H. Miyamoto, F. Kanamaru, S. Kume, and M. Koizumi, J. Inorg. Nucl. Chem. **34**, 1599 (1972).
15. H. Seki, T. Saito, and Y. Shimakawa, J. Jpn. Soc. Powder and Powder Metall. **63**, 609 (2016).
16. L. Wang, Z. Yang, X. Yin, S. D. Taylor, X. He, C. S. Tang, M. E. Bowden, J. Zhao, J. Wang, J. Liu, D. E. Perea, L. Wangoh, A. T. S. Wee, H. Zhou, S. A. Chambers, Y. Du, Sci. Adv. **7**, eabe2866 (2021).

17. L. Wang, Z. Yang, M. E. Bowden, J. W. Freeland, P. V. Sushko, S. R. Spurgeon, B. Matthews, W. S. Samarakoon, H. Zhou, Z. Feng, M. H. Engelhard, Y. Du, S. A. Chambers, Adv. Mater. **32**, 2005003 (2020).
18. S. Cook, T. K. Andersen, H. Hong, R. A. Rosenberg, L. D. Marks, and D. D. Fong, APL Mater. **5**, 126101 (2017).
19. See Supplemental Material at [] for details on Experimental Methods, Code availability, High-resolution XRD θ-2θ scans for the n =1 SL and the STNO solid solution, X-ray reflectivity, HAADF STEM image and corresponding individual EELS maps, Illustration of TEMWizard processing, and Ti L-edge, which includes Refs. [42–44].
20. K. Song, T. Min, J. Seo, S. Ryu, H. Lee, Z. Wang, S.-Y. Choi, J. Lee, C.-B. Eom, and S. H. Oh, Adv. Sci. **8**, 2002073 (2021).
21. G. Van der Laan, J. Zaanen, G. A. Sawatzky, R. Karnatak, and J.-M. Esteva, Phys. Rev. B **33**, 4253 (1986).
22. P. S. Bagus, M. J. Sassi, K. M. Rosso, J. Electron Spectrosc. Relat. Phenom. **200**, 174 (2015).
23. P. S. Bagus, E. S. Ilton, and C. J. Nelin, Surf. Sci. Rep. **68**, 273 (2013).
24. F. MF de Groot, H. Elnaggar, F. Frati, R.-P. Wang, M. U. Delgado-Jaime, M. V. Veenendaal, J. Fernandez-Rodriguez, M. W. Haverkort, R. J. Green, and G. van der Laan, J. Electron Spectrosc. Relat. Phenom. **249**, 147061 (2021).
25. L. Qiao, H. Y. Xiao, S. M. Heald, M. E. Bowden, T. Varga, G. J. Exarhos, M. D. Biegalski, I. N. Ivanov, W. J. Weber, T. C. Droubay, S. A. Chambers, J. Mater. Chem. C **1**, 4527 (2013).
26. R. Qiao, L. A. Wray, J.-H. Kim, N. PW Pieczonka, S. J. Harris, and W. Yang, J. Phys. Chem. C **119**, 27228 (2015).
27. N. Lu, P. Zhang, Q. Zhang, R. Qiao, Q. He, H.-B. Li, Y. Wang, J. Guo, D. Zhang, Z. Duan, Z. Li, M. Wang, S. Yang, M. Yan, E. Arenholz, S. Zhou, W. Yang, L. Gu, C.-W. Nan, J. Wu, Y. Tokura, and P. Yu, Nature **546**, 124 (2017).
28. S. Nemrava, D. A. Vinnik, Z. Hu, M. Valldor, C.-Y. Kuo, D. A. Zherebtsov, S. A. Gudkova, C.-T. Chen, L. H. Tjeng, and R. Niewa, Inorg. Chem. **56**, 3861 (2017).
29. M. Kotiuga, Z. Zhang, J. Li, F. Rodolakis, H. Zhou, R. Sutarto, F. He, Q. Wang, Y. Sun, Y. Wang, N. A. Aghamiri, S. B. Hancock, L. P. Rokhinson, D. P. Landau, Y. Abate, J. W. Freeland, R. Comin, S. Ramanathan, and K. M. Rabe, Proc. Natl. Acad. Sci. U.S.A. **116**, 21992 (2019).
30. L. Wang, Y. Du, P. V. Sushko, M. E. Bowden, K. A. Stoerzinger, S. M. Heald, M. D. Scafetta, T. C. Kaspar, and S. A. Chambers, Phys. Rev. Materials **3**, 025401 (2019).
31. J. W. Freeland, M. V. Veenendaal, and J. Chakhalian, J. Electron Spectrosc. Relat. Phenom. **208**, 56 (2016).
32. L. Wang, L. Chang, X. Yin, L.You, J.-L. Zhao, H. Guo, K. Jin, K. Ibrahim, J. Wang, A. Rusydi, J. Wang, Appl. Phys. Lett. **110**, 043504 (2017).
33. J.-S. Lee, Y. W. Xie, H. K. Sato, C. Bell, Y. Hikita, H. Y. Hwang, and C.-C. Kao, Nat. Mater. **12**, 703 (2013).
34. S. Roychoudhury, R. Qiao, Z. Zhuo, Q. Li, Y. Lyu, J.-H. Kim, J. Liu, E. Lee, B. J. Polzin, J. Guo, S. Yan,Y. Hu, H. Li, D. Prendergast, and W. Yang, Energy Environ. Mater. **4**, 246 (2021).
35. J. Chakhalian, J. M. Rondinelli, J. Liu, B. A. Gray, M. Kareev, E. J. Moon, N. Prasai, J. L. Cohn, M. Varela, I.-C. Tung, M. J. Bedzyk, S. G. Altendorf, F. Strigari, B. Dabrowski, L. H. Tjeng, P. J. Ryan, and J. W. Freeland, Phys. Rev. Lett. **107**, 116805 (2011).
36. E. A. Kraut, R. W. Grant, J. R. Waldrop, and S. P. Kowalczyk, Phys. Rev. Lett. **44**, 1620 (1980).
37. S. J. May, T. S. Santos, and A. Bhattacharya, Phys. Rev. B **79**, 115127 (2009).
38. R. Scherwitzl, S. Gariglio, M. Gabay, P. Zubko, M. Gibert, and J.-M. Triscone, Phys. Rev. Lett. **106**, 246403 (2011).
39. H. Wei, M. Jenderka, M. Bonholzer, M. Grundmann, and M. Lorenz, Appl. Phys. Lett. **106**, 042103 (2015).
40. J. Chaloupka and G. Khaliullin, Phys. Rev. Lett. **100**, 016404 (2008).

41. E. Cho, K. Klyukin, S. Ning, J. Li, R. Comin, R. J. Green, B. Yildiz, and C. A. Ross, Phys. Rev. Materials **5**, 094413 (2021).

42. L. Jones, H. Yang, T. J. Pennycook, M. S. J. Marshall, S. Van Aert, N. D. Browning, M. R. Castell and P. D. Nellist, Adv. Struct. Chem. Imaging **1**, 8 (2015).

43. M. Nord, P. E. Vullum, I. MacLaren, T. Tybell and R. Holmestad, Adv. Struct. Chem. Imaging **3**, 9 (2017).

44. M. Grinberg, Flask Web Development: Developing Web Applications with Python. ("O"Reilly Media, Inc.", 2018).

Figures and Figure captions

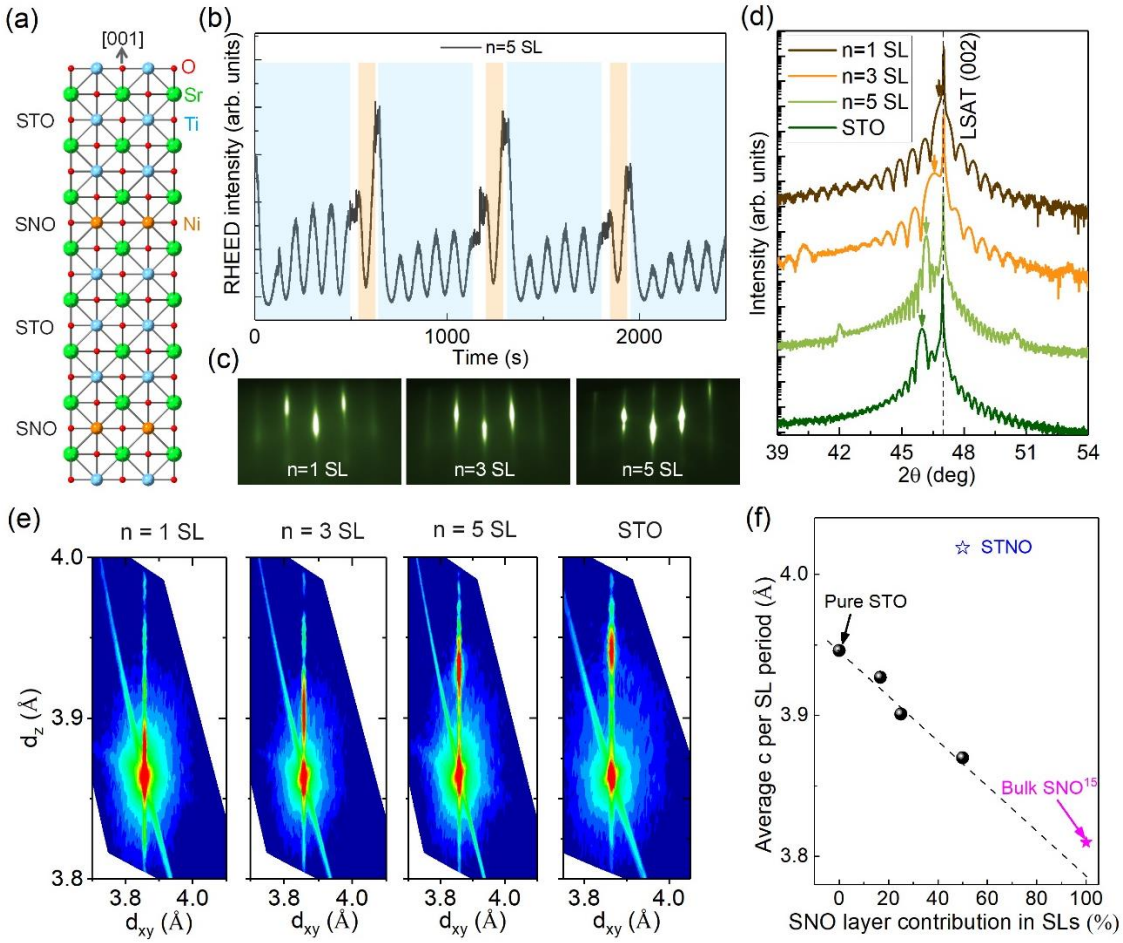

Figure 1. Synthesis of epitaxial $(SNO_1/STO_n)_k$ SLs and structural characterization. (a) Schematic diagram showing that one unit cell SNO is confined in the SLs with STO. (b) RHEED intensity oscillations of the specular reflected beam during the growth of the n = 5 SL. Blue-shaded areas mark the deposition of STO and yellow-shaded areas mark the deposition of SNO. (c) RHEED patterns for three SLs after growth viewed along the [100] zone axis. (d) High-resolution XRD θ-2θ scans for these SLs and one pure STO film grown on the same substrate. The k values are 20, 9, and 20 for n = 1, 3, and 5 SLs, respectively. The LSAT substrate peaks are marked by a dashed line and arrows denote the main SL peaks and the (002) diffraction peak for the STO film. (e) RSM near the 103 reflections for n = 1, 3, 5 SLs and pure STO film, confirming structural coherence. (f) Average out-of-plane lattice constant c as a function of the SNO layer contribution in SLs. c values of the STNO solid solution and bulk cubic SNO are also included for comparison.

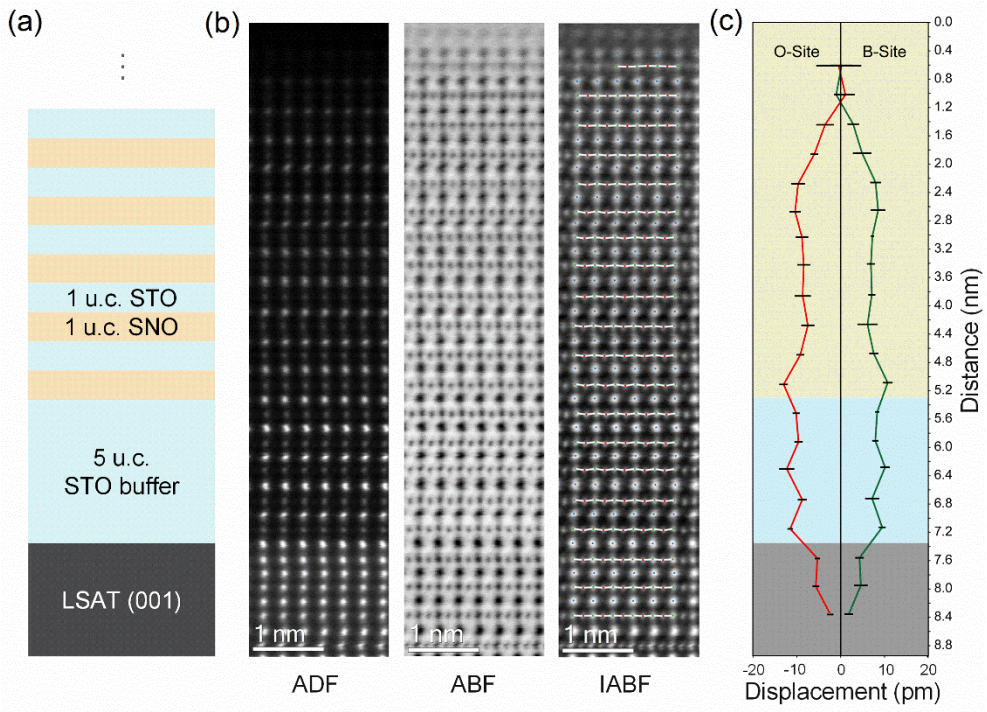

Figure 2. STEM analysis of interface structure and lattice distortions. (a) Structural diagram for the 5 u.c. STO-buffered $(SNO_1/STO_n)_k$ SL with $n = 1$. (b) Cross-sectional template-matched STEM ADF, ABF, and IABF images of the $n = 1$ SL along the [110] substrate orientation. Fitted bonds are overlaid on the IABF as white lines. (c) Average fitted B-site (green) and O (red) sublattice plane displacements relative to their mean as a function of distance from the surface.

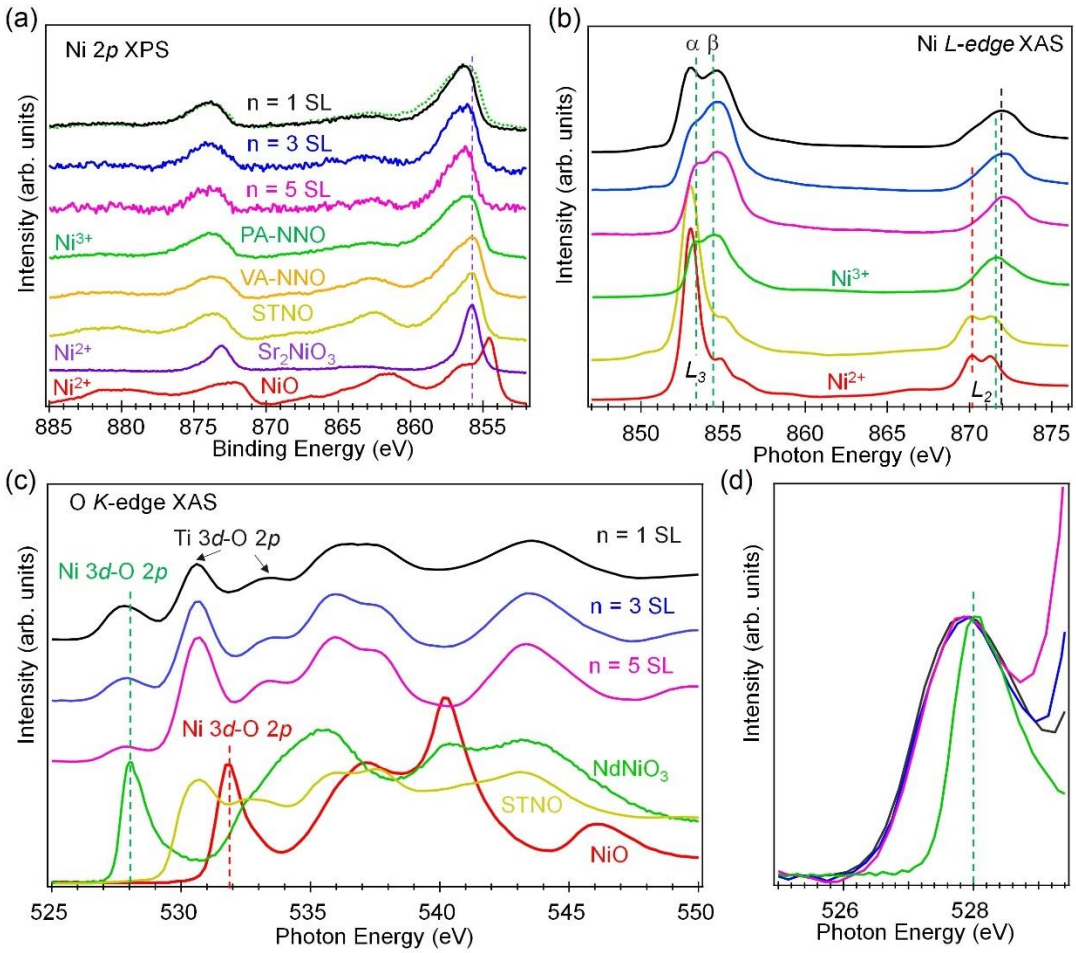

Figure 3. XPS and XAS results. The spectra of plasma annealed $NdNiO_3$ (PA-NNO), vacuum annealed $NdNiO_{3-\delta}$ (VA-NNO), Sr_2NiO_3, and NiO taken from ref. 16 are included for reference. (a) *In situ* Ni 2*p* XPS. The dashed purple lines denote the $2p_{3/2}$ binding energy for Sr_2NiO_3. For comparison, we overlay the Ni 2*p* spectrum of the PA-NNO (dotted black) on that of the $n = 1$ SL. (b) Ni *L*-edge XAS. The dashed red, green, and black lines denote the photon energy for Ni^{2+}, Ni^{3+} references, and the $n = 1$ SL, respectively. (c) O *K*-edge XAS. The dashed red and green lines denote the hybridization of the O 2*p* states with Ni 3*d* states. (d) Normalized pre-peak features in O *K*-edge XAS.

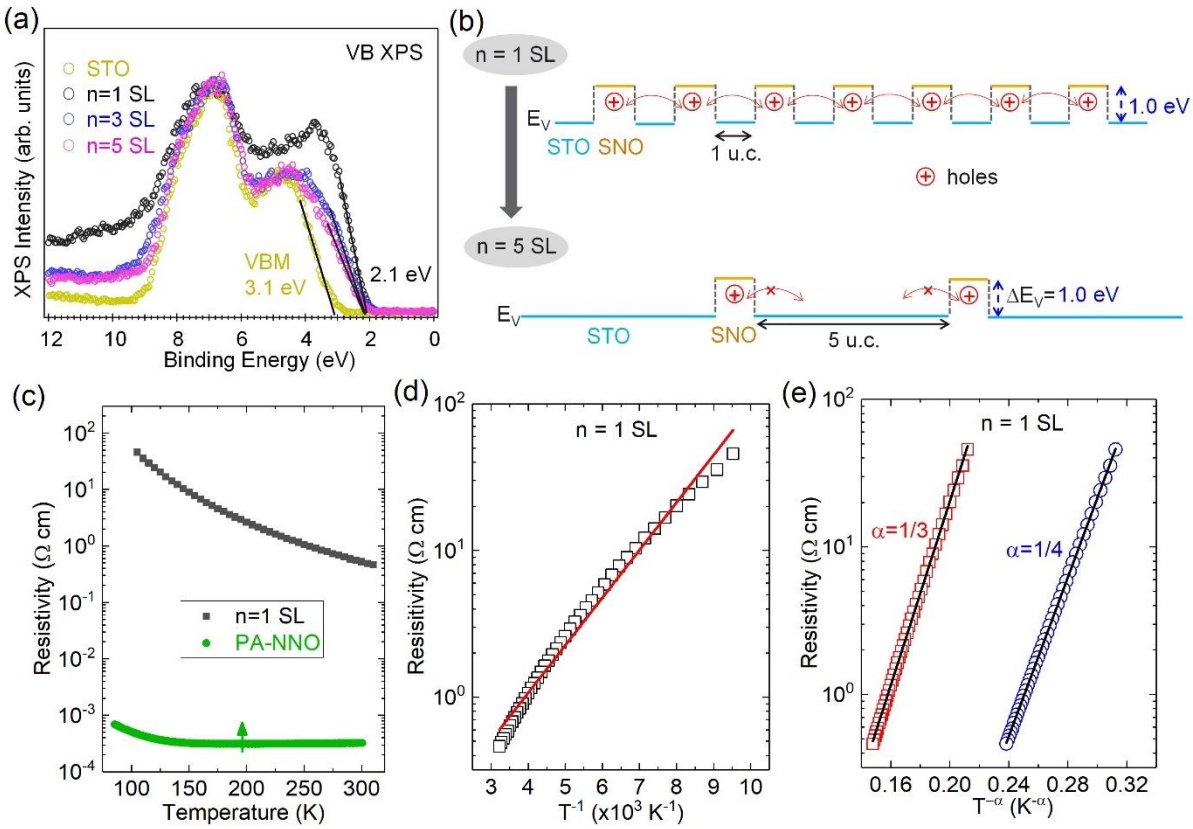

Figure 4. Valence band offset (VBO, ΔE_V) analysis and in-plane transport results. (a) VB spectra for pure STO film and SNO_1/STO_n SLs with *n* ranging from 1 to 5. Ti 2*p* spectra were used to align. VBMs are obtained by linear extrapolation of the leading edge to the energy axis. (b) Energy band-edge diagram for the STO_1/SNO_n SLs resulting from band alignment analysis. (c) Resistivity (ρ) vs. temperature curves on warming for the *n* = 1 SL and PA-NNO. (d) Resistivity as a function of 1/*T* over the range of 100-310 K. (e) Resistivity as a function of $T^{-\alpha}$ over the range of 100-310 K.